ACS APPLIED MATERIALS & INTERFACES

MnO Nanoparticles Interdispersed in 3D Porous Carbon Framework for High Performance Lithium-Ion Batteries

Shengbin Wang,[†,§] Yalan Xing,[†,§] Huaizhe Xu,[‡] and Shichao Zhang*[,†]

[†]School of Materials Science and Engineering, Beihang University, 37 Xueyuan Road, Beijing 100191, China
[‡]Center of Materials Physics and Chemistry, Beihang University, Beijing 100191, China

Ⓢ *Supporting Information*

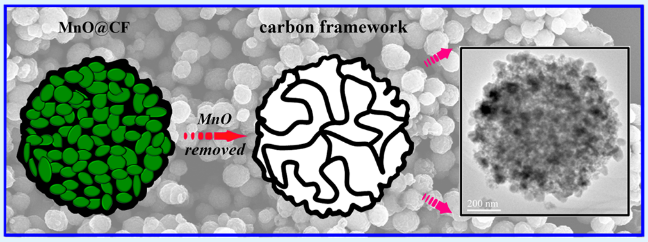

ABSTRACT: Interdispersed MnO nanoparticles that are anchored and encapsulated in a three-dimensional (3D) porous carbon framework (MnO@CF) have been constructed, which display nanosphere architecture with rich porosity, well-defined carbon framework configuration, and excellent structure stability. When evaluated as an anode material, the MnO@CF exhibits relatively high specific capacity of 939 mA h g^{-1} at current rate of 0.2 A g^{-1} over 200 cycles and excellent rate capability of 560.2 mA h g^{-1} at 4 A g^{-1}. By virtue of its mechanical stability and desirable ionic/electronic conductivity, the specific design can be a promising approach to fabricate high-performance lithium-ion batteries.

KEYWORDS: *MnO, interconnected carbon network, carbon framework, porous structure, lithium-ion batteries*

1. INTRODUCTION

There has been an increasing demand for long-term and high-performance rechargeable lithium-ion batteries (LIBs) for a wide range of applications from portable electronic devices to large-scale renewable energy power stations.[1−6] Graphite, with low cost, good cyclic stability, and low electrochemical potential, has been the most commonly used anode material for today's LIBs. However, the limited reversible intercalation capacity (with a theoretical capacity of 372 mA h g^{-1}) and poor rate performance have hindered its application for high-performance LIBs.[7] As a promising alternative to carbon-based anode, transition metal oxides (TMOs, M = Mn, Co, Fe) have been extensively investigated since the much higher reversible specific capacity could be achieved by their conversion reaction Li-storage mechanism.[8] Among various TMOs investigated for LIBs, MnO has attracted tremendous attention from researchers worldwide, owing to it being environmentally benign and the abundance of Mn,[9,10] as well as its relatively low conversion potential and voltage hysteresis in comparison with other TMOs.[11−14] In most cases, however, the application of MnO to practical LIBs is still largely hampered by their serious capacity fading upon cycling and/or poor rate capability, mainly ascribing to the large volume changes and/or poor electronic conductivity during Li-ion insertion/extraction.[15−17]

Current techniques to overcome these issues were particle down-sizing and surface carbon-incorporating to fabricate MnO/C nanocomposites,[15−20] which could improve the conductivity of Li-ions/electrons and accommodate the volumetric stress to enhance their electrochemical performance. However, the rate performance enhancement of such electrode materials is still limited, as the availability or percolation of the surface electronical conducting phase and/or the electrolyte become increasingly insufficient with the enhancing rate. Therefore, it still remains a great challenge to maintain and/or improve the electronic conductivity of MnO electrodes over continuous discharge/charge cycles.

Very recently, considerable interest has been focused on introducing a conductive network (such as carbon nanotubes[21−23] and graphene[24,25]) into electrode materials, which is a promising strategy to improve the electronic/ionic conductivity and the structural stability while enabling a high rate capability and excellent cyclability. For instance, Maier and co-workers introduced 3D conducting networks into electrode materials to shorten the electronic paths that exhibit significant enhancement of the rate performances.[26,27] However, it is still a challenge to restrain the severe volume expansion and aggregation during the cycling processes. Therefore, one promising design to further improve or optimize the electrochemical performance is to encapsulate and anchor the MnO nanoparticles in a 3D hierarchical conductive framework, in which both the surface conductive shell and interconnected conductive network are simultaneously constructed to effectively enhance the availability/penetrability of the conducting phase and the diffusion kinetics of ions/electrons.

In this study, interdispersed MnO nanoparticles that are encapsulated in three-dimensional (3D) porous carbon framework (MnO@CF) were synthesized, as illustrated in Figure 1. The 3D carbon framework with a dense network of pores serves as "electronic wire", which provides abundant diffusion pathways to favor fast transportation of Li-ions and electrons

Received: May 3, 2014
Accepted: July 14, 2014
Published: July 14, 2014

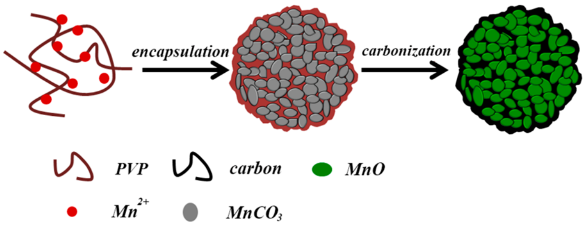

Figure 1. Schematic illustration for the synthesis of MnO@CF.

during electrochemical process. Moreover, the 3D carbon framework with structure stability could efficaciously accommodate the volume changes by providing bounteously elastic buffer space. Owing to the superior structural advantages, the resulting composite as a LIB anode exhibited a relative high reversible capacity, impressive rate capability, and significantly improved cycling performance in comparison with the traditional TMOs electrode.

2. EXPERIMENTAL SECTION

2.1. Synthesis of MnO@CF. Amounts of 1.5 g of $MnSO_4{\cdot}H_2O$ and 2 g of polyvinylpyrrolidone (PVP, $M_w \sim 1\,300\,000$) are dissolved into 200 mL of deionized water under stirring. Then, the NH_4HCO_3 solution with 7.9 g of NH_4HCO_3, 100 mL of deionized water, and 20 mL of ethanol is added to the mixed solution with vigorous stirring. The mixture is kept under stirring for 1 h. After adding 3 g of PVP into the solution, it is kept stirring for another 1 h. The $MnCO_3$@PVP nanospheres are obtained by suction filtration. The synthesized products are dried at 80 °C. Finally, the MnO@CF is obtained by heating at 700 °C for 2 h with a heating rate of 3 °C min^{-1}.

2.2. Surface and Structural Characterization. Powder X-ray diffraction data are collected on a Rigaku D/Max-2400 diffractometer with Cu Kα radiation. Scanning electron microscopy (SEM, Hitachi S-4800), transmission electron microscopy (TEM, JEM-2100F), and high-resolution transmission electron microscopy (HR-TEM, FEI, Tecnai G2 F20) are used to investigate the morphnology and microstructure of the sample. The specific surface area is determined by nitrogen adsorption−desorption at 77 K using a Quantachrome Autosorb-1C-VP analyzer. Thermogravimetric analysis (TGA) is performed on a NETZSCH STA 449C thermal analyzer under air atmosphere at a heating rate of 10 °C min^{-1}. The carbon and nitrogen contents are measured by using a Vario EL cube organic element analyzer. The Raman spectra are acquired on a labRAM ARAMIS laser Raman spectroscopy under a backscattering geometry (λ = 532 nm). X-ray photoelectron spectra (XPS) are recorded on a Thermo VG ESCALAB250 X-ray photoelectron spectrometer.

2.3. Electrochemical Characterization. The electrochemical experiments are performed using Coin-type cells (CR 2032) with lithium foil as the anode. The working electrode is fabricated with 80% MnO@CF, 10% acetylene black and 10% PVDF binder with active material loading of around 2.5 mg cm^{-2}. Cell are assembled in an argon filled glovebox with an electrolyte of 1 mol L^{-1} $LiPF_6$ in ethylene carbonate/dimethyl carbonate (EC/DMC = 1:1, volume ratio) solution and a separator of Celgard 2400. Electrochemical data are collected using NWEARE BTS-610 test system within the potential range of 0.01−3.0 V (vs Li^+/Li). A CHI 660D electrochemical workstation is employed for cyclic voltammograms (CV) tests at a scan rate of 0.1 mV s^{-1} between 0.01 and 3.0 V vs Li^+/Li. Electrochemical impedance spectra (EIS) are recorded on a Zahner IM6e electrochemical workstation at room temperature, in the frequency range from 10 MHz to 10 mHz.

3. RESULTS AND DISCUSSION

3.1. Structural Characteristics of MnO@CF. The fabrication process of MnO@CF is displayed in Figure 1. Manganese sulfate, ammonium bicarbonate, and PVP react in solution to produce the $MnCO_3$/PVP nanosphere precursors with a diameter of ∼800 nm (Figure S1, Supporting Information). During the heat treatment in a N_2 atmosphere, the $MnCO_3$ transforms to MnO nanoparticles, while PVP could decompose into the 3D porous carbon framework. Finally, the MnO@CF that MnO nanoparticles interdispersed in the carbon framework are successfully obtained. The XRD pattern of the product in Figure S2 shows that the peaks could be readily indexed to a well-crystallized cubic phase of MnO (JCPDS card no. 07-0230). The broad, low intensity diffraction peak in the range of 15−30° is likely associated with the presence of carbon. From the SEM images (Figure 2a,b), the well-dispersed spherical structure is preserved after heat treatment, and shows no obvious morphology change comparing to $MnCO_3$/PVP precursor. As shown in the TEM image (Figure 2c), MnO@CF nanospheres have a uniform spherical morphology with a particle size similar to that of SEM results. It clearly depicts that the MnO@CF nanosphere is composed of MnO primary nanocrystals of ∼50 nm. Interestingly, after a careful observation, the external porous feature of MnO@CF nanospheres can be also found, which could be attributed to the pyrolysis of the $MnCO_3$ and PVP during the heat treatment. The HR-TEM image in Figure 2d reveals that the nanospheres are coated by an external carbon sheath with a thickness around 4−7 nm. It demonstrates a core−shell nanoarchitecture where MnO nanocrystals are interdispersed and encapsulated in the carbon sheath. In addition, it has been reported that the core−shell composites with thin carbon layers (<3 nm) or thick carbon shell (>8 nm) are usually unfavorable to deliver an optimal capacity and cycle stability.[19,28,29] For the MnO@CF, the covered carbon with 4−7 nm thickness may be suitable to restrain the large volume stress and achieve an optimal electrochemical performance.

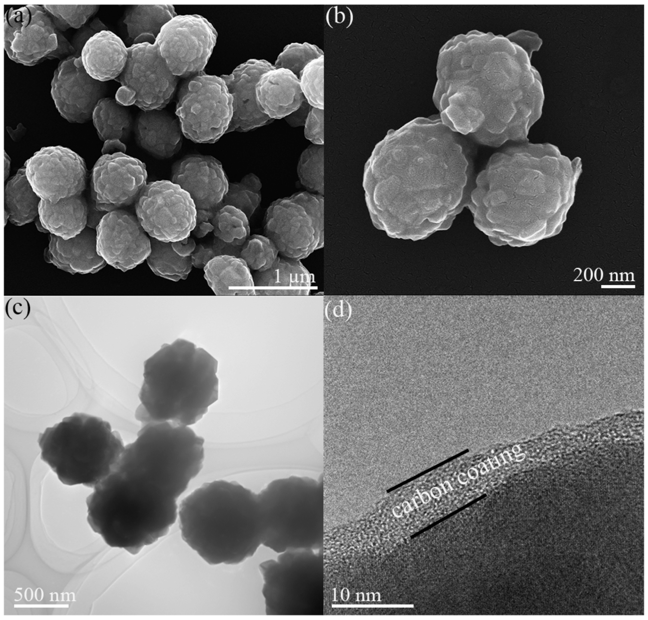

Figure 2. (a,b) SEM images, (c) TEM image, and (d) HR-TEM image of the MnO@CF.

The Brunauer−Emmett−Teller (BET) specific surface area and porosity property of the MnO@CF are studied by nitrogen adsorption−desorption analysis (Figure S3a). The BET specific surface area is measured to be about 57.3 m^2 g^{-1} with a pore volume of 0.35 cm^3 g^{-1}. The pore size distribution plot of the inset in Figure S3a demonstrates the presence of bimodal porosity: mesopores and macropores. Such porous structure is helpful for the good contact of MnO with electrolyte, and enhancement of diffusion kinetics in the solid state.[20,30] Thermogravimetric analysis (TGA) is carried out in air to determine the carbon content. In Figure S3b, a weight loss of 10.4% between 100 and 700 °C can be detected, which is attributed to the integrative effect of the weight loss (combustion of carbon to CO_2) and the weight gain (oxidation of MnO). Based on the theoretical value (11.3%) of the weight increase from MnO to Mn_2O_3, the carbon content in the MnO@CF is evaluated to be about 23.7 wt %.

For comparison, MnO nanospheres with carbon coated only on the surface (S-MnO@C) are synthesized and the morphology and structure are investigated (Figure S4). Comparing with MnO@CF, S-MnO@C shows worse dispersibility and lower specific surface area (13.9 $m^2\ g^{-1}$). In addition, the pore size distribution of S-MnO@C indicates only mesopores formed in the sample.

To investigate the carbon framework, MnO is removed from the MnO@CF using concentrated hydrochloric acid. After corrosion, SEM images (Figure S5a and b) show that the spherical structure is well kept with abundant interspace. The XRD pattern (Figure S5c) demonstrates that MnO is removed and the residual was carbon material. The TEM image after MnO removal is shown in Figure 3a. It is clear that many obvious bright regions appear in the sphere, revealing an underlying hierarchical porous structure which is consistent with the SEM result in Figure S5. From Figure 3a, it is demonstrated that MnO nanoparticles are interdispersed and encapsulated in the 3D porous carbon framework, as represented schematically in Figure 3b. Moreover, the BET measurement (Figure S5d) confirms that the surface area after MnO removal is 3 times higher than the originals (171.2 and 57.3 $m^2\ g^{-1}$, respectively), further implying the material changes and the hierarchical porous structure of the 3D carbon framework. Interestingly, the carbon matrix as revealed in Figure 3a (inset) demonstrates that the carbon framework is not absolutely amorphous but partically graphitized because of the clear lattice image, which is quite similar to that in our previous report.[2] The graphitic crystalline structure is further proved by the Raman spectrum (Figure 3c). The ratio ($R = I_G/I_D$) of the intensity of the G-band to the intensity of the D-band is estimated to be 1.29, indicating a relatively high degree of graphitic crystalline structure.[31] The graphite-like carbon framework not only could offer the good electrical conductivity, but also keep the structural integrity of the MnO@CF upon repeated cycling. Due to the N-containing carbon source of PVP, the composition of carbon framework is investigated by XPS. A pronounced N 1s peak is observed clearly for the carbon framework (Figure S6), which confirms the successful incorporation of N atoms into the carbon structure. In Figure 3d, three centered components resolved from the N 1s peak at ~398.6, ~400.3, and ~401.4 eV, representing pyridinic (N1), pyrrolic (N2), and graphitic (N3) type of N atoms, respectively. The nitrogen content of carbon framework is confirmed by organic elemental analyzer to be about 8.26 wt %, while that of the carbon is 82.89 wt %. Because of the raise of the Fermi level and surplus of electron after N-doping,[32−35] the graphite-like carbon framework will exhibit unusual properties in the electronic conductivity.

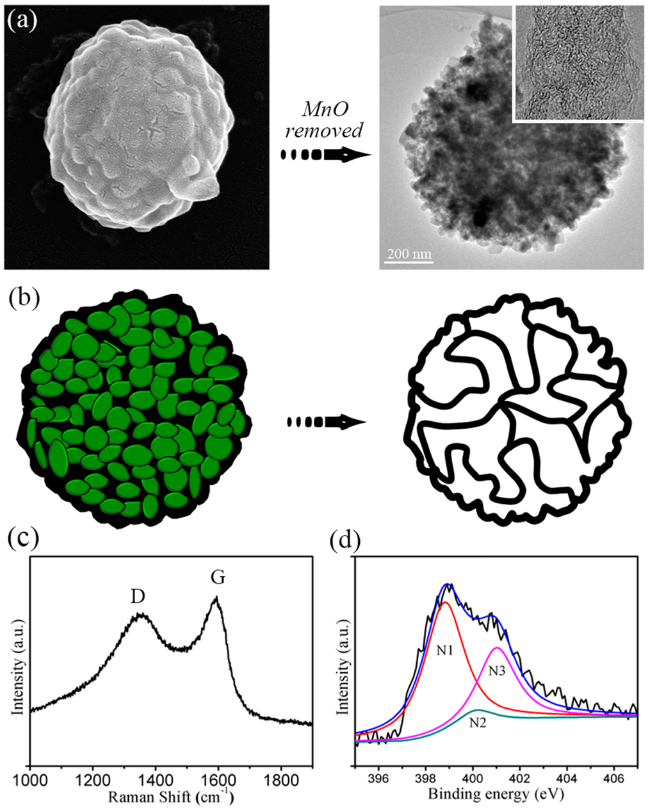

Figure 3. (a) Morphonology images; the inset is a HR-TEM image of carbon. (b) Schematic representation of the MnO@CF nanospheres before and after MnO removal. (c) Raman spectrum and (d) N 1s XPS spectra of the carbon framework.

3.2. Electrochemical Performance of the MnO@CF.

The electrochemical properties of MnO@CF are investigated by reversible deintercalation and intercalation of Li-ions between 0.01 and 3.0 V. The specific capacity is calculated based on the total weight of electrode material; that is, the carbon weight is included. The discharge/charge curves at 0.2 A g^{-1} in Figure 4a shown an initial specific discharge capacity around 1080 mA h g^{-1}, and the initial reversible charge capacity drops to 832 mA h g^{-1} with an initial Coulombic effciency as high as 77%. According to previous reports,[2,18] the irreversible capacity loss in the first two cycles can be attributed to the formation of solid electrolyte interphase (SEI) layer and/or some drastic Li-driven structural/textural changes. After 200 discharge/charge cycles, a high reversible discharge capacity of 939 mA h g^{-1} can be obtained. This gravimetric capacity is much higher than the theoretical capacities of both graphite (372 mA h g^{-1}) and MnO (755 mA h g^{-1}). Moreover, the Coulombic efficiency increased to almost 100% after the first cycle (Figure 4b). The excellent cycling performance indicates that the MnO@CF could reversibly react with Li-ions, and retain a stable structure even after continuous discharge/charge cycles (Figure S7).

The rate performance at the current densities from 0.2 to 4 A g^{-1} are examined, as shown in Figure 4c and d. As seen in Figure 4c, the gradually enlarged voltage hysteresis at higher currents are observed, which may be caused by the kinetic-limited effects of the electrochemical conversion reaction in nature.[20] From Figure 4d, it could be clearly observed that the MnO@CF delivers a discharge capacity of 786.7, 752.4, and 708.2 mA h g^{-1} at relatively small current rates of 1, 1.5, and 2 A g^{-1}, respectively. Even at the high rates of 3 and 4 A g^{-1}, competitive discharge capacities of 646.0 and 560.2 mA h g^{-1} can be maintained, respectively. The discharge capacities remain stable and decrease regularly with the increasing rates, indicating

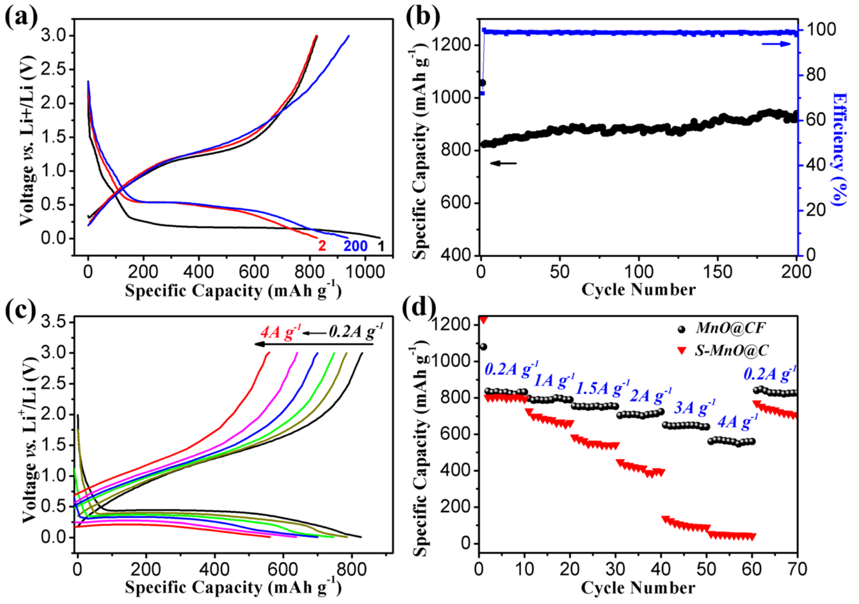

Figure 4. (a) Charge−discharge profiles, (b) cycling performance and Coulomb efficiency of the MnO@CF electrode at current density of 0.2 A g^{-1}. (c) Charge−discharge profiles of MnO@CF. (d) Rate performance of MnO@CF and S-MnO@C at various current densities from 0.2 A g^{-1} to 4 A g^{-1}.

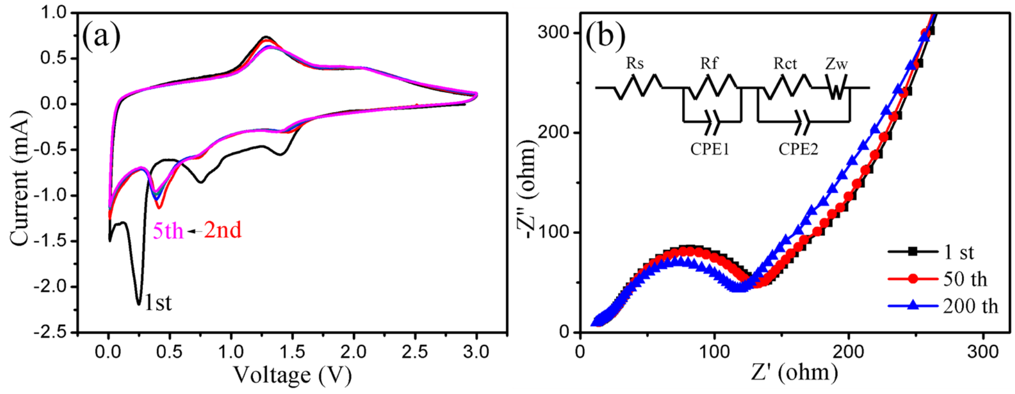

Figure 5. (a) CV curves of MnO@CF obtained at a scan rate of 0.1 mV s^{-1} in the voltage range of 0.01−3 V. (b) EIS spectra after different discharge/charge cycles at 0.2 A g^{-1}. Inset of (b) is the equivalent circuit used.

a good kinetic feature and facile charge transport process of the MnO@CF. Furthermore, it is noticed that a satisfactory reversible capacity of 837.6 mA h g^{-1} could be recovered after 60 cycles upon reducing the current rate to 0.2 A g^{-1} (Figure 4d), indicating an excellent rate performance that the rate capacity is maintainable even after the repetitive cycles at high rates.

For comparison, the electrochemical performance of S-MnO@C is also investigated. It is found that the capacity of the S-MnO@C fades to 708.2 mA h g^{-1} at the 200th cycle, though its initial capacity is close to MnO@CF (Figure S8). Meanwhile, in Figure 4d, it could be clearly seen that the reversible capacity of S-MnO@C shows a sharp decline with increasing current density, and retains little capacity at a high rate of 4 A g^{-1}. The results demonstrate that the improvement in electrochemical performance of the MnO@CF, in terms of cycling performance and rate capability, should be attributed to the 3D N-doped graphite-like carbon framework structure.

To understand the superior electrochemical performance of the MnO@CF electrode, CV and EIS studies are carried out to investigate the physical/chemical behavior during the discharge/charge cycling. In Figure 5a, a cathodic peak at 1.4 V in the first cycle can be assigned to the reduction of Mn^{3+} or Mn^{4+} to Mn^{2+}, which could be originated from a trace of Mn_xO_y impurity from the partial oxidation of the Mn^{2+} in the MnO@CF.[15] In addition, the reduction peaks at 0.75 and 0.24 V correspond to the formation of solid electrolyte interface (SEI) layer and the irreversible decomposition of electrolyte.[15,16] From the second cycle onward, the sharp peak at 0.42 V in the anodic sweep and the smooth peak at about 1.3 V in the cathodic sweep could be ascribed to the reversible redox conversion reaction between lithium and MnO to form Mn^0 and Li_2O (Li^0 + MnO → Li_2O + Mn^0).[16,18] The excellent reversibility of curves in the following cycles reveals the improvement of reaction kinetics and structure stability after the first lithiation. It is worth noting that an oxidation peak at ∼2.11 V becomes evident in the following cycles, which is also reflected in Figure 4a that may correspond to the decomposition of the polymer/gel layer at high oxidation potential above 2.0 V,[15] and/or the Mn^{2+} reoxidized to a higher oxidation state.[16,18] The electrochemical impedance spectra of the MnO@CF (Figure 5b) and S-MnO@C (Figure S9) are investigatd. The Nyquist plots of MnO@CF of different cycles shows similar shapes, exhibiting a good cycling stability. An equivalent circuit model base on the EIS result is built up as shown in the inset of

Figure 5b. The intercept of the high-frequency semicircle on the Z' axis can be attributed to the resistance of electrolyte (R_s). R_f and R_{ct} are the resistance of the SEI layer and the charge transfer, respectively. The slope line at low frequency is related to Warburg impedance (Z_w), corresponding to the diffusion of lithium ions into the bulk electrode. The fitting values of kinetic parameters of MnO@CF and S-MnO@C electrodes are listed in Table S1. It is worth noting that the R_{ct} of MnO@CF is much lower, about half of its counterpart, implying much faster charge transfer at the electrode/electrolyte interface. This result further demonstrates that the 3D N-doped graphite-like carbon framework in the MnO@CF serves as a conductive pathway, as illustrated in Figure 6, ensuring the effective ambipolar diffusion of Li-ions and electrons in the interfaces of electrolyte/electrode.[36]

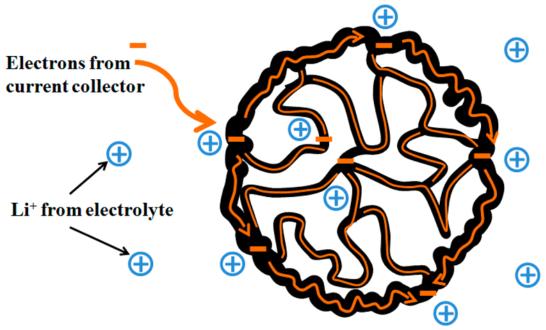

Figure 6. Schematic conduction/diffusion of electrons and Li ions within the MnO@CF particles.

4. CONCLUSIONS

In summary, interdispersed MnO nanoparticles anchored and encapsulated in a 3D porous carbon framework are successfully fabricated. When evaluated as the anode material for LIBs, the MnO@CF exhibits high specific capacity and rate capability, and excellent cycling stability. The construction of MnO@CF induced a simultaneous improvement in several electrochemical key parameters, which can be understood by the following reasons. The 3D porous N-doped graphite-like carbon framework could create abundant percolated conductive pathways to effectively facilitate Li-ion/electron transfer by its electrochemical reactivity and electronic conductivity. In addition, the good elasticity and mechanical stability of this 3D carbon structure could effectively buffer the internal stress caused by volume variation of MnO materials accompanying Li-ion insertion/extraction processes. By virtue of its superior structural advantages, the specific 3D conductive framework design can be a promising approach to fabricate high-performance LIBs.

■ ASSOCIATED CONTENT

Ⓢ Supporting Information

SEM images, XRD patterns, XPS spectrum, discharge/charge curves, and EIS spectra. This material is available free of charge via the Internet at http://pubs.acs.org.

■ AUTHOR INFORMATION

Corresponding Author

*E-mail: csc@buaa.edu.cn.

Author Contributions

§S.W. and Y.X. contributed equally.

Notes

The authors declare no competing financial interest.

■ ACKNOWLEDGMENTS

This work was supported by the National Basic Research Program of China (973 Program) (2013CB934001), National Natural Science Foundation of China (51074011 and 51274017), and National 863 Program (2007AA03Z231 and 2011AA11A257).

■ REFERENCES

(1) Tarascon, J. M.; Armand, M. Issues and Challenges Facing Rechargeable Lithium Batteries. *Nature* **2001**, *41*, 359−367.

(2) Wang, S.; Ren, Y.; Liu, G.; Xing, Y.; Zhang, S. Peanut-like MnO@C Core−Shell Composites as Anode Electrodes for High-Performance Lithium Ion Batteries. *Nanoscale* **2013**, *6*, 3508−3512.

(3) Goodenough, J. B.; Park, K.-S. The Li-Ion Rechargeable Battery: A Perspective. *J. Am. Chem. Soc.* **2013**, *135*, 1167−1176.

(4) Xing, Y.; Wang, Y.; Zhou, C.; Zhang, S.; Fang, B. Simple Synthesis of Mesoporous Carbon Nanofibers with Hierarchical Nanostructure for Ultrahigh Lithium Storage. *ACS Appl. Mater. Interfaces* **2014**, *6*, 2561−2567.

(5) Wu, H. B.; Chen, J. S.; Hng, H. H.; Lou, X. W. Nanostructured Metal Oxide-Based Materials as Advanced Anodes for Lithium-Ion Batteries. *Nanoscale* **2012**, *4*, 2526−2542.

(6) Liu, C.; Li, F.; Ma, L.; Cheng, H. Advanced Materials for Energy Storage. *Adv. Mater.* **2010**, *22*, E28−E62.

(7) Reddy, M. V.; Subba Rao, G. V.; Chowdari, B. V. R. Metal Oxides and Oxysalts as Anode Materials for Li Ion Batteries. *Chem. Rev.* **2013**, *113*, 5364−5457.

(8) Poizot, P.; Laruelle, S.; Grugeon, S.; Dupont, L.; Tarascon, J. M. Nano-Sized Transition-Metal Oxides as Negative-Electrode Materials for Lithium-Ion Batteries. *Nature* **2000**, *407*, 496−499.

(9) Gao, J.; Lowe, M. A.; Abruna, H. D. Spongelike Nanosized Mn_3O_4 as a High-Capacity Anode Material for Rechargeable Lithium Batteries. *Chem. Mater.* **2011**, *23*, 3223−3227.

(10) Zhang, K.; Han, P.; Gu, L.; Zhang, L.; Liu, Z.; Kong, Q.; Zhang, C.; Dong, S.; Zhang, Z.; Yao, J.; Xu, H.; Cui, G.; Chen, L. Synthesis of Nitrogen-Doped MnO/Graphene Nanosheets Hybrid Material for Lithium Ion Batteries. *ACS Appl. Mater. Interfaces* **2012**, *4*, 658−664.

(11) Zhang, L.; Wu, H. B.; Liu, B.; Lou, X. W. Formation of Porous SnO_2 Microboxes via Selective Leaching for Highly Reversible Lithium Storage. *Energy Environ. Sci.* **2014**, *7*, 1013−1017.

(12) Tan, L.; Pan, L.; Cao, C.; Wang, B.; Li, L. Nitrogen-Doped Carbon Coated TiO_2 Nanocomposites as Anode Material to Improve Cycle Life for Lithium-Ion Batteries. *J. Power Sources* **2014**, *253*, 193−200.

(13) Cui, Z.i-M.; Jiang, L.-Y.; Song, W.-G.; Guo, Y.-G. High-Yield Gas-Liquid Interfacial Synthesis of Highly Dispersed Fe_3O_4 Nanocrystals and Their Application in Lithium-Ion Batteries. *Chem. Mater.* **2009**, *21*, 1162−1166.

(14) Li, L.; Seng, K.; Chen, Z.; Guo, Z.; Liu, H. Self-assembly of Hierarchical Star-like Co_3O_4 Micro/Nanostructures and Their Application in Lithium Ion Batteries. *Nanoscale* **2013**, *5*, 1922−1928.

(15) Sun, B.; Chen, Z.; Kim, H.-S.; Ahn, H.; Wang, G. MnO/C Core-Shell Nanorods as High Capacity Anode Materials for Lithium-Ion Batteries. *J. Power Sources* **2011**, *196*, 3346−3349.

(16) Sun, Y.; Hu, X.; Luo, W.; Xia, F.; Huang, Y. Reconstruction of Conformal Nanoscale MnO on Graphene as a High-Capacity and Long-Life Anode Material for Lithium Ion Batteries. *Adv. Funct. Mater.* **2013**, *23*, 2436−2444.

(17) Luo, W.; Hu, X.; Sun, Y.; Huang, Y. Controlled Synthesis of Mesoporous MnO/C Networks by Microwave Irradiation and Their Enhanced Lithium-Storage Properties. *ACS Appl. Mater. Interfaces* **2013**, *5*, 1997−2003.

(18) Guo, J.; Liu, Q.; Wang, C.; Zachariah, M. R. Interdispersed Amorphous MnO_x-Carbon Nanocomposites with Superior Electrochemical Performance as Lithium-Storage Material. *Adv. Funct. Mater.* **2012**, *22*, 803−811.

(19) Li, X.; Xiong, S.; Li, J.; Liang, X.; Wang, J.; Bai, J.; Qian, Y. MnO@ Carbon Core-Shell Nanowires as Stable High-Performance Anodes for Lithium-Ion Batteries. *Chem.—Eur. J.* **2013**, *19*, 11310−11319.

(20) Xia, Y.; Xiao, Z.; Dou, X.; Huang, H.; Lu, X.; Yan, R.; Gan, Y.; Zhu, W.; Tu, J.; Zhang, W.; Tao, X. Green and Facile Fabrication of Hollow Porous MnO/C Microspheres from Microalgaes for Lithium-Ion Batteries. *ACS Nano* **2013**, *7*, 7083−7092.

(21) Bülow, J. F.; Zhang, H.; Morse, D. E. Hydrothermal Realization of High-Power Nanocomposite Cathodes for Lithium Ion Batteries. *Adv. Energy Mater.* **2012**, *2*, 309−315.

(22) Li, X.; Kang, F.; Bai, X.; Shen, W. A Novel Network Composite Cathode of $LiFePO_4$/Multiwalled Carbon Nanotubes with High Rate Capability for Lithium Ion Batteries. *Electrochem. Commun.* **2007**, *9*, 663−666.

(23) Sun, X.; Xu, Y.; Ding, P.; Chen, G.; Zheng, X.; Zhang, R.; Li, L. The Composite Sphere of Manganese Oxide and Carbon Nanotubes as a Prospective Anode Material for Lithium-Ion Batteries. *J. Power Sources* **2014**, *255*, 163−169.

(24) Wang, H.; Cui, L.; Yang, Y.; Casalongue, H. S.; Robinson, J. T.; Liang, Y.; Cui, Y.; Dai, H. Mn_3O_4-Graphene Hybrid as a High-Capacity Anode Material for Lithium Ion Batteries. *J. Am. Chem. Soc.* **2010**, *132*, 13978−13980.

(25) Sun, Y.; Hu, X.; Luo, W.; Huang, Y. Self-Assembled Hierarchical MoO_2/Graphene Nanoarchitectures and Their Application as A High-Performance Anode Material for Lithium-Ion Batteries. *ACS Nano* **2011**, *5*, 7100−7107.

(26) Hu, Y.-S.; Liu, X.; Muller, J.-O.; Schlogl, R.; Maier, J.; Su, D. S. Synthesis and Electrode Performance of Nanostructured V_2O_5 by Using a Carbon Tube-in-Tube as a Nanoreactor and an Efficient Mixed-Conducting Network. *Angew. Chem., Int. Ed.* **2009**, *48*, 210−214.

(27) Guo, Y.-G.; Hu, Y.-S.; Sigle, W.; Maier, J. Superior Electrode Performance of Nanostructured Mesoporous TiO_2 (Anatase) through Efficient Hierarchical Mixed Conducting Networks. *Adv. Mater.* **2007**, *19*, 2087−2091.

(28) Ding, Y.; Wu, C.; Yu, H.; Xie, J.; Cao, G.; Zhu, T.; Zhao, X.; Zeng, Y. Coaxial MnO/C Nanotubes as Anodes for Lithium-Ion Batteries. *Electrochim. Acta* **2011**, *56*, 5844−5848.

(29) Liu, Y.; Zhao, X.; Li, F.; Xia, D. Facile Synthesis of MnO/C Anode Materials for Lithium-Ion Batteries. *Electrochim. Acta* **2011**, *56*, 6448−6452.

(30) Vu, A.; Qian, Y. Q.; Stein, A. Porous Electrode Materials for Lithium-Ion Batteries−How to Prepare Them and What Makes Them Special. *Adv. Energy Mater.* **2012**, *2*, 1056−1085.

(31) Shanmugam, S.; Gedanken, A. MnO Octahedral Nanocrystals and MnO@C Core−Shell Composites: Synthesis, Characterization, and Electrocatalytic Properties. *J. Phys. Chem. B* **2006**, *110*, 24486−24491.

(32) Sheng, Z.-H.; Shao, L.; Chen, J.-J.; Bao, W.-J.; Wang, F.-B.; Xia, X.-H. Catalyst-Free Synthesis of Nitrogen-Doped Graphene via Thermal Annealing Graphite Oxide with Melamine and Its Excellent Electrocatalysis. *ACS Nano* **2011**, *5*, 4350−4358.

(33) Czerw, R.; Terrones, M.; Charlier, J. C.; Blase, X.; Foley, B.; Kamalakaran, R. Identification of Electron Donor States in N-Doped Carbon Nanotubes. *Nano Lett.* **2001**, *1*, 457−460.

(34) Wu, Z.; Ren, W.; Xu, L.; Li, F.; Cheng, H. Doped Graphene Sheets As Anode Materials with Superhigh Rate and Large Capacity for Lithium Ion Batteries. *ACS Nano* **2011**, *5*, 5463−5471.

(35) Paraknowitsch, J. P.; Thomas, A. Doping Carbons Beyond Nitrogen: An Overview of Advanced Heteroatom Doped Carbons with Boron, Sulphur and Phosphorus for Energy Applications. *Energy Environ. Sci.* **2013**, *6*, 2839−2855.

(36) Li, H.; Zhou, H. Enhancing the Performances of Li-Ion Batteries by Carbon-Coating: Present and Future. *Chem. Commun.* **2012**, *48*, 1201−1217.